Atmos. Chem. Phys. Discuss., 14, 31441–31481, 2014
www.atmos-chem-phys-discuss.net/14/31441/2014/
doi:10.5194/acpd-14-31441-2014

Atmospheric Chemistry and Physics Discussions

Aging of secondary organic aerosol from small aromatic VOCs: changes in chemical composition, mass yield, volatility and hygroscopicity

L. Hildebrandt Ruiz[1,2], A. L. Paciga[2,*], K. Cerully[3,], A. Nenes[3], N. M. Donahue[2], and S. N. Pandis[2,4]**

[1]The University of Texas at Austin, Austin, Texas, USA
[2]Carnegie Mellon University, Pittsburgh, Pennsylvania, USA
[3]Georgia Institute of Technology, Atlanta, Georgia, USA
[4]University of Patras, Patras, Greece
[*]now at: Phillips66®, Bartlesville, OK, USA
[**]now at: TSI, Inc., Shoreview, MN, USA

Received: 3 November 2014 – Accepted: 11 November 2014 – Published: 12 December 2014

Correspondence to: L. Hildebrandt Ruiz (lhr@che.utexas.edu)

Published by Copernicus Publications on behalf of the European Geosciences Union.

Abstract

Secondary organic aerosol (SOA) is transformed after its initial formation, but this chemical aging of SOA is poorly understood. Experiments were conducted in the Carnegie Mellon environmental chamber to form and transform SOA from the photo-oxidation of toluene and other small aromatic volatile organic compounds (VOCs) in the presence of NO_x. The effects of chemical aging on organic aerosol (OA) composition, mass yield, volatility and hygroscopicity were explored. Higher exposure to the hydroxyl radical resulted in different OA composition, average carbon oxidation state ($\overline{OS}_C$) and mass yield. The OA oxidation state generally increased during photo-oxidation, and the final OA $\overline{OS}_C$ ranged from −0.29 to 0.45 in the performed experiments. The volatility of OA formed in these different experiments varied by as much as a factor of 30, demonstrating that the OA formed under different oxidizing conditions can have significantly different saturation concentration. There was no clear correlation between hygroscopicity and oxidation state for this relatively hygroscopic SOA.

1 Introduction

Secondary organic aerosol (SOA) is produced when gas-phase precursors are oxidized, forming lower volatility products that partition to the condensed phase. As SOA is estimated to account for approximately 70 % of total aerosol organic carbon mass (Hallquist et al., 2009), the influence of SOA on aerosol composition and related properties is important and complex (Donahue et al., 2009; Kanakidou et al., 2005; Kroll and Seinfeld, 2008). Using measurements in urban, suburban, and remote sites, Zhang et al. (2007) showed that as aerosol ages in the atmosphere it reaches a highly oxidized state and no longer resembles either fresh primary or secondary aerosol.

Although it is clear that oxidation of gas-phase compounds and continued oxidation of particle-phase compounds play an important role in SOA production and transformation, the underlying chemistry and thermodynamics are poorly understood. With-

ACPD
14, 31441–31481, 2014

out the correct representation of SOA production and evolution mechanisms, modeling attempts often lead to underestimations of ambient mass loadings (Heald et al., 2005; Volkamer et al., 2006). The large uncertainty in SOA concentrations predicted by Chemical Transport Models (CTMs) demonstrates the need for experimental data on the multi-generation oxidation reactions or "aging" that directly lead to changes in mass loadings and chemical properties of SOA. Several computational studies have highlighted the importance of not only incorporating extended chemical mechanisms but obtaining corresponding relationships between aging and physiochemical properties, such as volatility, in atmospherically relevant systems (Cappa and Wilson, 2012; Shrivastava et al., 2013).

Considering the current state-of-the-science in aerosol analysis techniques, identifying the plethora of SOA components and their individual volatilities is not possible. A unified framework to evaluate complex systems in field or laboratory studies and to track changes in volatility as a function of aging is the 2D-Volatility Basis Set (2D-VBS). It uses coordinates of volatility in terms of effective saturation concentration, C^*, and oxidation state of carbon, $\overline{OS}_C$ (or the oxygen to carbon ratio ratio, O : C) to provide a space suitable for the description of the chemical transformations and phase partitioning of aerosols (Donahue et al., 2012). Chemical species are lumped by C^* and $\overline{OS}_C$ in discretized bins.

The relationship between organic aerosol hygroscopicity and oxidation, indicated by O : C, has been the focus of a number of laboratory and field studies (Alfarra et al., 2013; Chang et al., 2010; Frosch et al., 2011; Jimenez et al., 2009; Lambe et al., 2011; Lathem et al., 2013; Massoli et al., 2010). While organic aerosol hygroscopicity often increases with O : C, other studies have found weak or no correlation between the two properties (Alfarra et al., 2013; Frosch et al., 2011; Lathem et al., 2013; Massoli et al., 2010). It has been shown that $\overline{OS}_C$ is likely a better indicator of aerosol oxidation than O : C as the latter can be affected by non-oxidative processes such as hydration and dehydration while $\overline{OS}_C$ increases continually with oxidation (Canagaratna et al.,

ACPD
14, 31441–31481, 2014

2014; Kroll et al., 2009, 2011); thus, O : C may not be as well correlated with observed hygroscopicity.

The presence of surfactants affects the ability of particles to act as CCN, hence their observed hygroscopicity. For supersaturated conditions, critical supersaturation (and hence the hygroscopicity parameter κ) is affected by changes in surface tension considerably more than for subsaturated conditions (Ruehl et al., 2010). A large body of research (Asa-Awuku et al., 2008; Engelhart et al., 2008; Facchini et al., 1999, 2000; King et al., 2009; Li et al., 2011; Padro et al., 2007, 2010; Ruehl et al., 2012; Shulman et al., 1996; Topping et al., 2007) suggests that surface tension from dissolved solute in the aerosol can vary by about 10 % at the point of activation. These soluble compounds can either preexist in the dry aerosol or form from dissolution of compounds, like methylglyoxal, from the gas-phase (Li et al., 2011; Lim et al., 2013; Sareen et al., 2010). Recently, gas-phase compounds have also been suggested to adsorb directly on the droplet-air interface and affect surface tension, increasing the apparent hygroscopicity of inorganic seed aerosol (Sareen et al., 2013).

The increased aerosol hygroscopicity with increased oxidation has been proposed to be further linked with decreased aerosol volatility (Jimenez et al., 2009). While few chamber studies have investigated the link among all three properties (Poulain et al., 2010; Tritscher et al., 2011), several additional studies have shown that the relationship between volatility and hygroscopicity may not be as straightforward (Asa-Awuku et al., 2009; Cerully et al., 2009; Meyer et al., 2009; Tang et al., 2012). These investigations encompass both subsaturated (Meyer et al., 2009; Tritscher et al., 2011) and supersaturated (Asa-Awuku et al., 2009; Cerully et al., 2014; Poulain et al., 2010; Tang et al., 2012) conditions. Asa-Awuku et al. (2009) and Tang et al. (2012) found that in chamber experiments involving SOA formed from β-caryophyllene the most volatile fraction was also the most hygroscopic. In chamber studies of α-pinene SOA, Meyer et al. (2009) also measured a decrease in hygroscopicity with increased volatility. Poulain et al. (2010) found that the most volatile components of α-pinene SOA were also the most hygroscopic, in agreement with Asa-Awuku et al. (2009), Cerully

ACPD
14, 31441–31481, 2014

et al. (2014), Meyer et al. (2009), and Tang et al. (2012), though contradictory to the conventional view that the most volatile components should be the least hygroscopic. Additionally, Poulain et al. (2009) found that the most oxygenated aerosol showed lower volatility than the less oxygenated aerosol, in agreement with the conventional view. Tritscher et al. (2011) found that hygroscopicity and O : C remained constant with decreased volatility for α-pinene SOA during aging by OH radicals.

We investigated the relationship between oxidation, volatility and hygroscopicity of SOA formed from the photo-oxidation of toluene under a variety of oxidation conditions. A main objective is to connect the extent of oxidation and the changes in volatility of these experiments with the 2D-VBS framework.

2 Materials and methods

2.1 Environmental chamber experiments

Organic aerosol was formed from the photo-oxidation of toluene and other small aromatic VOCs in the Carnegie Mellon Center for Atmospheric Particle Studies (CAPS) environmental chamber. The basic sequence of the experiments was to fill the chamber with clean air, inject the VOC and nitrous acid (HONO), and turn on the UV lights to start formation of OH (from the photolysis of HONO), oxidation of the VOC and formation of secondary organic aerosol (SOA). The number of UV lights used, the initial VOC concentrations, and the number of HONO injections was varied between experiments in order to create different oxidizing environments, as summarized in Table 1. The amount of SOA formed, the SOA oxidation state, its volatility and its hygroscopicity were then measured as explained in more detail below.

Nitrous acid was produced immediately before injection by drop-wise addition of 12 mL 0.1 M sodium nitrite solution to 24 mL 0.05 M sulfuric acid solution. Ammonium sulfate ($(NH_4)_2SO_4$, Sigma Aldrich, 99.99 %) seed particles were used in some experiments (Table 1) to provide surface area onto which organics would condense as SOA.

ACPD
14, 31441–31481, 2014

In the unseeded experiments, nucleation of the organic vapors was observed. With the exception of Experiment 7 (Table 1), isotopically labeled toluene was used (^{13}C-toluene, Cambridge Isotope Laboratories, 99 %) as in a previous study (Hildebrandt et al., 2011). All six ring carbons in the labeled toluene are ^{13}C-substituted, leaving the methyl carbon unsubstituted. Concentrations of the VOCs were monitored using a proton-transfer reaction mass spectrometer (PTR-MS, Ionicon Analytik GmbH) when available. PTR-MS measurements of toluene were corrected for ion-source intensity and humidity as suggested by de Gouw et al. (2003). The sensitivity of the PTR-MS to the VOCs was measured before each experiment using a calibration gas mixture; calculated sensitivities agreed well with VOC concentrations expected based on the volume of liquid VOC injected.

Figure 1 presents the experimental setup. Particle number and volume of the chamber aerosol were measured using a scanning mobility particle sizer (SMPS), comprised of a TSI model 3080 classifier and a TSI model 3772 condensation particle counter (CPC). Particle mass and chemical composition was measured using a high-resolution time-of-flight aerosol mass spectrometer (AMS) from Aerodyne, Inc. (DeCarlo et al., 2006). The AMS has two ion optical modes named by the shape of the ion flight paths: a single-reflection mode (V-mode) with a shorter flight path and hence higher sensitivity but lower resolution, and a double-reflection mode (W-mode) with longer flight path and hence higher resolution but lower sensitivity. In this study the AMS was operated according to the common protocol with the vaporizer temperature at 600 °C, alternating between V and W modes to collect mass spectra, and collecting particle time-of-flight (pToF) measurements in V-mode.

Air from the chamber was split into two separate streams for analysis of OA concentrations and properties. In the first stream, OA volatility was probed using a thermodenuder (TD) system, similar to the system used in Lee et al. (2010). Aerosol was passed alternately through the TD, heated to a predefined temperature, or a bypass line and then to the SMPS and the AMS for measurements of the particle size distributions and chemical composition. Properties of thermally-treated OA were determined

ACPD
14, 31441–31481, 2014

by comparing the residual aerosol after heating in the TD to the aerosol which was passed through the bypass line. The standard operating sample flowrate for the TD was 1 $Lmin^{-1}$ (LPM), corresponding to a centerline residence time of ~ 15 s. In the TD followed by the AMS, the flow rate was also sometimes set to 0.6 LPM, corresponding to a centerline residence time of ~ 25 s, to evaluate the effects of a longer residence time on OA evaporation, though these data were not used for thermally-denuded CCN comparisons. In the second stream, aerosol was again passed alternately through the TD or bypass line, then size-selected (approximately 100 to 140 nm) using a differential mobility analyzer (DMA, TSI model 3080) operated with a sheath to aerosol ratio of 10 : 1. Aerosol flow was then split to a CPC (TSI model 3010) and a cloud condensation nuclei counter (CCNc, Droplet Measurement Technologies). The CCNc was operated in Scanning Flow CCN Analysis (SFCA) mode (Moore and Nenes, 2009), allowing for fast measurements of CCN by scanning the flow rate through the CCNc column, which measured the OA hygroscopicity. The thermodenuder positioned before the CCNc operated under the same temperature conditions as the AMS-TD and had a sample flowrate of 1 LPM, which allows for analysis of volatility and hygroscopicity of the complete OA and the thermally denuded OA. Dilution air of 1.1 LPM was introduced after the DMA before splitting to the CCNc and CPC. Flow to the CCNc was held constant at 1.1 LPM using a laminar flow element, while flow in the CCNc was linearly ramped between 0.1 and 0.9 $L\,min^{-1}$ over 60 s. The top to bottom column temperature difference was 6 °C for all experiments.

2.2 AMS data analysis

The AMS data were processed in Igor Pro 6.12 (Wavemetrics, Inc.) using the standard AMS data analysis toolkits "Squirrel" version 1.51C for unit mass resolution (UMR) analysis and "Pika" version 1.10C for high resolution (HR) analysis. HR analysis was performed using the W-mode data since highest resolution is preferred to distinguish between isotopically labeled and unlabeled ions. The lists of ions integrated in the HR analysis is similar to the list used previously (Hildebrandt et al., 2011). Molecular ions

ACPD
14, 31441–31481, 2014

were fitted up to an m/z ratio of 105; above this the signal was too noisy and/or the mass spectra were too crowded for reliable identification of ion atomic composition. According to the UMR analysis more than 95 % of the organic signal was below m/z 105, and the total organic mass was corrected based on this fraction calculated for each experiment (Table S1 in the Supplement). The natural abundance of ^{13}C (1.112 %) was accounted for by constraining the mass attributed to fragments containing one ^{13}C based on the concentration of the parent ^{12}C fragments, only attributing any excess signal to ^{13}C-toluene SOA. Ions with two or more ^{13}C were not isotopically constrained since their natural abundance is very low and does not significantly affect results.

2.2.1 Modification of standard fragmentation table

Several adjustments were made to the standard fragmentation table (Allan et al., 2004) for the analysis of HR and UMR data as explained in detail in the Supplement; only the most important adjustments are summarized here. First, the fragmentation table was adjusted to account for H-atoms ($m/z = 1$) formed in the fragmentation of H_2O (Canagaratna et al., 2014). Second, the amount of H_2O^+ attributed to organics was chosen so that the mass of water does not correlate with the mass of organics ($R < 0.01$) as expected for these low relative humidity experiments. The ratios of organic H_2O^+ to ($^{13}CO_2^+ + CO_2^+$) are provided in Table 2 and ranged from 0.3 to 2.4, higher than the ratio of 0.225 in the default fragmentation table but consistent with recent calibration experiments (Canagaratna et al., 2014). Third, since no inorganic nitrate is added to or expected to be formed in these experiments, ions assigned to the nitrate family in the HR analysis (NO^+, NO_2^+) are presumed to be due to organic nitrates and were added to the total organic aerosol mass in the HR batch table. Nitrate fragments were not included in the calculation of O : C and H : C since elemental analysis examines the oxidation state of the carbon atoms.

ACPD
14, 31441–31481, 2014

2.2.2 Ionization efficiency, airbeam and V vs. W modes

Data were corrected for changes in the instrument airbeam (AB) over the course of an experiment. The ionization efficiency (IE) for each experiment was adjusted based on the ratio of the AB during the experiment to the AB during the ionization efficiency calibration conducted before this set of experiments was started (calibration IE/AB = 4.65×10^{-13}). Total aerosol concentrations were calculated in the following way to exploit the higher sensitivity (and accuracy) in V-mode and the higher resolution in W-mode. First, UMR fragmentation and batch tables were used to obtain bulk concentration data for sulfate in V and W mode. The V/W ratio was then computed for sulfate, obtaining a measure of the difference in total concentrations measured in these two modes. Second, HR analysis and the HR fragmentation and batch tables were used to obtain organic and sulfate concentrations in W-mode. The W-mode HR data were then multiplied by the (V/W) ratio (from UMR analysis) to obtain the most quantitative estimate of the amount of organic and sulfate mass detected by the AMS. Because all sulfate in these experiments is from the ammonium sulfate seed particles, sulfate mass was multiplied by 1.375 to obtain ammonium sulfate mass. Using the V/W ratio as a correction factor indirectly applies an AB correction in W-mode. When sulfate data were not available, nitrate concentrations in V and W mode were used instead to compute the V/W ratio. The AB and V/W ratio used to correct the data in each experiment are shown in Table S1.

2.2.3 Determination of collection efficiency

A further issue with all AMS analysis is that the AMS does not detect all sampled particles, primarily due to particle bounce at the vaporizer. The AMS collection efficiency (CE) for these data was estimated by matching AMS mass distributions and SMPS volume distributions using the OA density (ρ_{org}) and AMS CE as fitting parameters, with the algorithm developed by Kostenidou et al. (2007). Particle time of flight (pToF) distributions of organics and sulfate (SO_4^{2-}) from V-mode were used but scaled by the

ACPD
14, 31441–31481, 2014

adjusted HR aerosol masses (from MS mode) obtained as described above. The pToF distributions were smoothed before fitting using a 19-point, 2nd order Savitzky–Golay smoothing.

The data from each experiment were split according to whether the OA had been passed through the bypass or the TD to observe whether the denuded OA had a different CE and/or density compared to the total OA. The data from Expt. 9 were further split into a total of 16 periods to explore variation in CE and OA density over the course of an experiment (e.g., with increasing OH exposure of the OA or different denuder temperatures). As can be seen in Fig. S1 in the Supplement, the CE and OA density did not change significantly over the course of an experiment. There is also very little difference in CE between the OA passed through the bypass or the thermodenuder (Table S1, all experiments). As observed earlier (Lee et al., 2010) the algorithm for estimating AMS CE and OA density is much less sensitive to the OA density than to the AMS CE, and the estimated CE essentially remains the same after fixing the OA density at 1.5 g cm^{-3} (Fig. S1). The values of CE are used to correct OA concentrations for the calculation of OA mass yield and mass fraction remaining. Values of OA density are used to convert aerodynamic to mobility diameter for CCN analysis.

2.2.4 Quantifying organic aerosol production

The amount of organic aerosol formed was quantified as the fractional aerosol mass yield (mass of OA formed divided by mass of toluene reacted). The mass of OA formed needs to be corrected for the depositional loss of particles onto the chamber walls, and for the condensational loss of organic vapors to wall-deposited particles. The assumption is made that condensation of organic vapors is not slowed by mass-transfer resistances, and that the wall-deposited particles are in equilibrium with the organic vapors in suspension. Therefore, the total (corrected) concentration of OA can be calculated by multiplying the OA/seed ratio by the initial seed concentration, as discussed in more detail in a previous publication (Hildebrandt et al., 2009).

ACPD
14, 31441–31481, 2014

2.3 Analysis of organic aerosol volatility

2.3.1 Data preparation

Volatility data were collected for each experiment after the SOA had formed. During some experiments, measurements were also made during the irradiation period (with the UV lights on) to examine the volatility changes during photo-oxidation. TD data are analyzed in terms of Volume Fraction Remaining (VFR) or Mass Fraction Remaining (MFR). Using the total organic mass concentration from the AMS, the MFR was calculated by dividing the mass concentration of the denuded OA by the mass concentration of the OA that had passed through the bypass. These data are presented in the form of a thermogram, which shows the MFR as a function of temperature in the TD.

Particle concentrations decline in the smog chamber after SOA formation chemistry ceases due to losses to the chamber walls. This can lead to biases in the estimated MFR when bypass concentrations before or after the TD sampling period are used. A more accurate MFR was obtained by interpolation of the bypass OA concentrations corresponding to the TD sampling times. Each experiment was analyzed individually for a best fit, usually resulting in an exponential decay function. Graphs of the interpolated bypass data are shown in Fig. S2.

Particle losses in the TD were also taken into account. These losses occur due to diffusion (primarily of small particles), sedimentation (primarily of large particles), and thermophoresis; the losses are therefore a function of sample flow rate, temperature, and particle size (Burtscher et al., 2001). To estimate the losses within the TD setup, size dependent loss functions were developed using NaCl particles under various TD temperatures and sample flow rates (Lee and Pandis, 2010). The number losses for each TD temperature – residence time combination are calculated by determining the losses over the size distribution measured by the SMPS. The number losses for each size bin are then converted to a volume-based correction using the particle diameter of each bin. This correction factor is applied to the calculated MFR values. The organic MFR was calculated from AMS bypass and thermodenuder mass concentrations av-

ACPD
14, 31441–31481, 2014

eraged over 6–9 min for a given TD temperature and residence time. It is assumed that there are no significant changes to composition and volatility over these averaging periods.

2.3.2 Evaporation model

Due to the non-equilibrium conditions in the TD, a dynamic mass transfer model developed by Riipinen et al. (2010) was used to estimate the relative volatility of the OA formed in the experiments outlined in Table 1. Briefly, aerosol evaporation is simulated using experimental inputs including TD temperature, residence time, particle mode diameter, mass concentration, and OA density. This method utilizes the volatility basis set approach (Donahue et al., 2006) to account for the component complexity in the SOA formed. Assuming the particles are in equilibrium with the vapor phase as they enter the TD, the effective saturation concentration is estimated from a least-squares fit to the experimental thermograms. An important caveat to this approach is that physical properties including mass accommodation coefficient and enthalpy of vaporization, which are usually unknown, can substantially affect the volatility estimated (Lee et al., 2010). The primary goal of these experiments was to observe changes in OA volatility with different levels of oxidation. Thus, relative volatility changes were calculated as described below, thus reducing uncertainties arising from the choice of accommodation coefficient and enthalpy of vaporization.

The volatility of SOA formed in each experiment was determined assuming a fixed volatility distribution shape using four saturation concentrations, 1, 10, 100, and 1000 $\mu g\,m^{-3}$. During the analysis the saturation concentrations are multiplied by a shifting factor, s. This practically shifts the volatility distribution to lower or higher values assuming that the shape of the distribution does not change. The shifting factors can then be interpreted as differences in volatility of the OA formed in different experiments. The volatility distribution used is based on the fresh toluene SOA distribution estimated by Hildebrandt et al. (2009) for their high NO_x experiments: 0.025 for C^* = 1, 0.51 for C^* = 10, 0.38 for C^* = 100, and 0.085 for C^* = 1000 $\mu g\,m^{-3}$. The shifting factor is esti-

ACPD
14, 31441–31481, 2014

mated for each of the experiments presented here by using the mass transfer model and least squares fitting to the MFRs. In the last step relative shifting factors are calculated by normalizing them by the shifting factor of the OA formed in Expt. 7, in which SOA had the lowest $\overline{OS}_C$. In this way, the relative volatility reduction (reciprocal of the shifting factor) for each experiment is estimated while accounting for the experiment specifics including residence time, TD temperature, mass concentration, and particle size. Fixed values are used for the enthalpy of vaporization (80 kJ mol^{-1}) and the mass accommodation coefficient (1.0). The sensitivity of results to these choices will be discussed in Sect. 3.2.

2.4 Analysis of CCN activity

2.4.1 CCNc calibration

The CCNc instrument calibration is used to determine the relationship between instantaneous instrument flow rate and supersaturation as described in Moore and Nenes (2009). Ammonium sulfate solution is atomized, dried using a silica gel diffusion dryer, charge-neutralized using Po-210, and classified by a DMA. The flow is then introduced into both a CPC and a CCNc. The activation ratio, or the ratio of CCN to total particles, is then plotted against the instantaneous flow rate to yield data that are fit to a sigmoidal activation ratio function. The critical flow rate, Q^*, is determined, corresponding to where half of the total particles are activated and to a level of supersaturation, s^*, equal to the critical supersaturation of the classified aerosol (Sect. 2.4.2). The Q^* and s^* are determined for a range of aerosol sizes, yielding, for the flow rate range (0.1–0.9 L min^{-1}) and temperature gradient (ΔT = 6 °C) in the CCNc column, supersaturations ranging from approximately 0.10 to 0.50 %.

ACPD
14, 31441–31481, 2014

2.4.2 Calculating aerosol hygroscopicity of size-selected aerosol

Using the method outlined in Sect. 2.4.1, s^* was determined for each flow rate upscan and downscan. All CCNc data subject to poor counting statistics (where the maximum CCN concentrations were lower than approximately 15 to 20 counts cm^{-3}) were excluded from analysis (Moore et al., 2010). The characteristic hygroscopicity parameter, κ (Petters and Kreidenweis, 2007), of the monodisperse CCN is then determined by

$$\kappa = \frac{4A^3}{27 d_p^3 s^{*2}} \quad (1)$$

where $A = (4M_w\sigma_w)/(RT\rho_w)$; M_w, σ_w, and ρ_w are the molar mass, surface tension, and density of water, respectively. R is the universal gas constant, T is CCNc mid-column temperature, and d_p is the dry particle diameter selected by the DMA prior to the CCNc.

3 Results and discussion

3.1 Organic aerosol concentration, composition and mass yield

Figure 2 shows the time series of OA concentrations and oxidation state for an unseeded experiment (2) and a seeded experiment (9). There were two photo-oxidation periods ("lights on") during each experiment, and HONO was injected every time before lights were turned on. During experiment 2, the OA was alternatively passed through the bypass and the TD throughout the experiment (only the bypass data are shown in Fig. 2). The TD was held at the same temperature during the photo-oxidation periods to observe changes in volatility during this period, and the temperature in the TD was varied during the dark period to obtain a thermogram. During experiment 9, the OA was passed only through the bypass during photo-oxidation, and it was alternated between bypass and TD (at different temperatures) during the dark period. The OA concentra-

ACPD
14, 31441–31481, 2014

tions increased during the oxidation periods (lights on) as toluene (not shown) was oxidized to form SOA.

The behavior of oxidation state was different for these two experiments. In Expt. 2 the oxidation state was initially very high (~ 3), consistent with very highly oxidized, low-volatility organic compounds nucleating to form new particles. After the initial formation of particles two competing effects can influence the OA oxidation state: first, according to partitioning theory, species of increasingly higher volatility will partition to the particle phase as the OA loading in the system increases. If oxidation state is anti-correlated with volatility this effect would decrease oxidation state when OA concentration increases. Second, the existing OA can be oxidized further (aged), increasing the OA oxidation state as long as the molecules composing the OA do not fragment. The oxidation state of the OA formed in Expt. 2 first decreased and then increased during both irradiation periods, suggesting that first the partitioning effect and then the aging effect dominated. In Expt. 9 and all other experiments conducted the oxidation state of the OA formed increased over the course of the experiments, suggesting that the aging effect always dominated. The OA formed in Expt. 2 had a much higher oxidation state than the OA formed in the other experiments (Table 2); hence it appears that the aging effect dominates in these experiments unless the OA oxidation state is already very high.

In an attempt to produce highly oxidized OA, photo-oxidation of the OA was continued for over 24 h during experiments 3 and 5. Figure 3 shows the time series of oxidation state and elemental ratios (O : C and H : C) for experiment 3. As before, HONO was injected before every irradiation period. A significant decrease in oxidation state and O : C was observed during the long irradiation period. Plausible explanations for this decrease in oxidation state include the condensation of less oxidized vapors, that OA components are photolyzed, or that they fragment after continued oxidation with OH. In the last two cases the fragmented products may have a high oxidation state but high volatility (due to their smaller size) and evaporate from the OA, decreasing the OA average oxidation state. Photolysis of organic compounds is expected to occur

ACPD
14, 31441–31481, 2014

throughout the experiment, but as long as OH reactions dominate the oxidation state of the bulk OA increases. Future experiments should aim to isolate OH from photolysis reactions by, for example, using a dark OH source. This would help to constrain these effects and eventually represent them in chemical transport models.

Table 2 provides a summary of the OA composition for all experiments investigated here. The observed oxidation state of the OA formed ranged from −0.29 to 0.45. At least 10 % of the OA mass was due to the sum of NO^+ and NO_2^+ ions. The observed ratio of NO^+ to NO_2^+ (Table 2) was between 7.0 and 8.6, much higher than typically observed ratios for NH_4NO_3 (Farmer et al., 2010), suggesting that the NO^+ and NO_2^+ ions originate from organic nitrogen (ON) compounds. Estimating that the ON compounds have an average molecular weight of about 200 g mol^{-1}, approximately half of the OA is due to ON. Thus, organic nitrogen compounds are a major constituent in the OA formed in these high-NO_x photo-oxidation experiments.

The HR data can shed light on the different roles of the methyl carbon atom (methyl-C) and the aromatic-Cs in the photo-oxidation reactions. (Recall that the aromatic-Cs on the ^{13}C-toluene are isotopically substituted but the methyl-C is not.) Table 2 lists the average ratio $CO_2 : {}^{13}CO_2$ for all experiments. In experiments 1–5 and experiment 9, only ^{13}C-toluene SOA was present in the system, so $^{12}CO_2$ originates from the methyl-C on ^{13}C-toluene. If the methyl-C behaved as the aromatic-Cs, the expected ratio of $CO_2 : {}^{13}CO_2$ would be 1/6. However, $CO_2 : {}^{13}CO_2$ is about threefold lower than this. The CO_2^+ fragment observed in AMS data is thought to originate primarily from organic acid functional groups; hence, this observation suggests that the methyl-C is about three times less likely than the aromatic-Cs to form organic acids in these photo-oxidation reactions.

3.2 High and low oxidation experiments – a case study

This section compares two seeded experiments (number 7 and 9, Table 1) and two unseeded experiments (number 2 and 4). The aim in the design of these experiments

ACPD
14, 31441–31481, 2014

was to create very different photochemical conditions. Therefore, less HONO and more toluene was injected, fewer lights were used (resulting in lower UV intensity), and the irradiation period was shorter in Expt. 7 compared to Expt. 9 (10 min and 3 h, respectively). The decay of toluene, monitored by the PTR-MS, was used to estimate the OH exposure of the OA during irradiation – total OH exposure during Expt. 7 was 7–8 times lower than during Expt. 9. Figure 4 shows the OA mass yields for experiments 7 and 9 as a function of the corrected OA concentration in the system. The OA yields are higher for Expt. 9, which exhibited higher OH exposure. The OA formed in Expt. 9 also exhibited significantly higher oxidation state (~ 0, Table 2) than the OA formed in Expt. 7 (~ -0.3), and its volatility was approximately a factor of seven lower than the volatility of the OA formed in Expt. 7 (Table 2). The SOA loading was approximately twice as high in Expt. 7 compared to Expt. 9. Higher OH exposure during Expt. 9 resulted in different OA composition, reflected in a higher oxidation state and lower volatility.

The OA mass yields shown in Fig. 4 are lower than high NO_x OA mass yield measured in our previous study (Hildebrandt et al., 2009), likely due to different initial and oxidizing conditions. In the previous study the source of OH and NO_x was HOOH and NO, and all NO converted to NO_2 within a few minutes of the start of photo-oxidation. In the present study the source of OH and NO_x was HONO, and both NO and NO_2 were present throughout the experiments. Gas-phase chemistry is primarily affected by the level of NO, not total NO_x, and lower OA mass yields are expected under high NO, high NO_x conditions (present study) compared to high NO_x low NO conditions (Hildebrandt et al., 2009).

Differences in the OA composition are also apparent when comparing the total OA to the denuded OA from these two experiments. Figure 5 (left panel) shows the difference in oxidation state of the denuded and the total OA at the different TD temperatures for Expt. 7 and 9. For the less oxidized, more volatile OA formed in Expt. 7, the oxidation state of the denuded OA is higher than the oxidation state of the total OA, as expected when volatility correlates with oxidation state. The difference is larger at the higher TD temperatures when a larger fraction of the total OA has evaporated. However, for the

ACPD
14, 31441–31481, 2014

more oxidized, less volatile OA formed in Expt. 9, the denuded OA has essentially the same oxidation state as the total OA at all TD temperatures. This is consistent with the OA being composed of molecules that have a similar oxidation state but different chain length, resulting in different volatilities. A similar observation was made when sampling highly oxygenated OA during ambient measurements in Finokalia, Greece, where the fraction of OA due to fragments of m/z 44 was not significantly different for denuded and total OA (Hildebrandt et al., 2010).

A similar comparison can be made for two non-seeded experiments (number 2 and 4), which resulted in OA of different oxidation state and volatility (Table 2). The experimental conditions were designed to be similar for these two experiments (Table 1); however, the HONO source is difficult to control, and it is likely that higher OH concentrations as well as lower OA concentrations in Expt. 2 resulted in the more oxidized, less volatile OA. Data from the PTR-MS were not available for this experiment, hence, OH exposure could not be estimated and OA mass yields could not be calculated. The OA formed in Expt. 4 had similar oxidation state as the OA formed in Expt. 9 mentioned above (~ 0). The OA formed in Expt. 2 had the highest oxidation state of all OA analyzed here (~ 0.45), and its volatility was about a factor of seven lower than the volatility of the OA formed in Expt. 4. The right panel of Fig. 5 shows the difference in oxidation state (denuded vs. total) as a function of TD temperature for Expts. 2 and 4. The OA formed in Expt. 4 exhibits similar behavior as the OA formed in Expt. 9, with very little difference between the oxidation state of denuded and total OA. The OA in Expt. 2 shows a higher oxidation state for denuded OA than for non-denuded OA. Thus, it appears that for OA of lower and higher bulk oxidation state, the oxidation state anti-correlates with volatility, shown here as a higher oxidation state of the denuded OA. For OA of intermediate oxidation state (around zero), the volatility of the OA does not correlate significantly with bulk oxidation state. The bulk oxidation state of OA formed in one experiment does not always correlate with its volatility. The OA volatility of all experiments is analyzed further below.

ACPD
14, 31441–31481, 2014

3.3 Volatility

Figure 6 shows mass concentration time series measured during Experiment 7 including both the bypass and TD measurements. This experiment produced the least oxidized and most volatile SOA and serves as the baseline for our analysis of volatility in the other experiments. HONO was injected into the chamber and, at $t = 0$, the UV lights (30 % of them) in the chamber were turned on. The hydroxyl radical formed during the HONO photolysis began to react with toluene and the organic mass concentration increased due to the formation of SOA. The lights remained on for approximately 15 min and at that point the HONO photolysis was stopped by turning off the UV lights. The AMS then alternated between the bypass line and thermodenuder (operating at different temperatures and residence times) to obtain the thermogram shown in Fig. 7. Half of the organic aerosol mass evaporated at 70 °C (T_{50} temperature). For this and all other experiments, the MFR was nearly the same after 15 and 25 s residence time in the thermodenuder.

The 15 and 25 s residence time datasets were independently modeled, resulting in two estimates of volatility reduction for each experiment. These were quite similar (Table 2) for all cases suggesting that these measurements are consistent with the choice of a unity accommodation coefficient. The estimated relative volatility reductions relative to Experiment 7 for all experiments are presented in Table 2, and the experiment-specific model inputs (OA loading, particle mode diameter, and OA density) are presented in Table S2. Volatility was lower in other experiments by as much as a factor of 30, demonstrating that the OA formed can have significantly different vapor pressure under different oxidation conditions. Figure 8 shows a comparison of the modeled vs. the measured MFRs.

To examine the effects of the accommodation coefficient and enthalpy of vaporization parameters, sensitivity runs were performed. In summary, the analysis revealed that changing the mass accommodation coefficients between 0.01, 0.1 and 1 for Expts. 7 and 9, which exhibited quite different experimental conditions, changes neither

ACPD
14, 31441–31481, 2014

the relative volatility reduction nor the goodness of fit (represented by the sum of squared residuals, SSR) by more than 15 %. In addition, better least squares fits are obtained for enthalpy of vaporization of 80 kJ mol^{-1} (average SSR for all nine experiments, SSR_{avg} = 0.04) than for enthalpy of vaporizations of 20 or 120 kJ mol^{-1} (SSR_{avg} = 0.11 and 0.09, respectively). Changing the enthalpy of vaporization does not change the trends in volatility reduction between experiments. Detailed results of the sensitivity study are presented in the Supplement (Tables S3 and S4).

3.3.1 Dependence of volatility on oxidation state

The change in volatility of the toluene SOA in these experiments can be compared to its oxidation state (Fig. 9). The change in volatility is expressed as the logarithm of the volatility reduction. This is consistent with the assumption of a constant volatility distribution shape shifting. Each data point represents a single experiment in terms of volatility reduction or the change in $\log C^*$ and the corresponding carbon oxidation state. In general, the more oxidized organic aerosol is less volatile. This is consistent with functionalization reactions decreasing the volatility of the OA as it is oxidized. Using a least squares fit, a straight line is fit to the dataset giving a relation of $(\overline{OS}_C) = 0.467(\Delta \log_{10} C^*) - 0.324$. This suggests that an increase of the oxidation state by approximately 0.5 units corresponds to a reduction of the average volatility by an order of magnitude for the toluene SOA system examined here. However, as we have noted above the volatility of individual species composing the OA is not always correlated to its oxidation state.

3.4 Hygroscopicity

CCNc-derived organic hygroscopicity, κ_{org}, expressed as the average hygroscopicity of all measured sizes, vs. the bulk O : C ratio and $\overline{OS}_C$ is shown in Fig. 10 for each experiment where CCNc data were available. Throughout all experiments, κ_{org} ranges from 0.10 to 0.25 while bulk O : C ranges from approximately 0.85 to 1.05. For each

ACPD
14, 31441–31481, 2014

experiment, after the initial period of photo-oxidation, κ_{org} remains fairly constant, as does O : C. There is no clear correlation between κ_{org} and O : C (Fig. 10 top, left) or between κ_{org} and $\overline{OS}_C$ (Fig. 10 top, right) across all experimental conditions. This is counter to the conventional view that oxidative aging of aerosol generally increases its hygroscopicity (Jimenez et al., 2009).

When investigating κ_{org} for Expts. 4 and 6 where both non-denuded and thermally-denuded measurements were collected, it appears that thermally-denuded aerosol (combined measurements from 60, 80, and 100 °C) may show a slight decrease in κ_{org} with increased O : C (and $\overline{OS}_C$) (Fig. 10 bottom). While the change in κ_{org} as well as O : C and $\overline{OS}_C$ cannot be concluded with confidence due to the relatively large variation in κ_{org}, it is possible that this relationship between hygroscopicity and oxidation suggests that there may be another process, aside from bulk oxidation changes, causing changes in the measured hygroscopicity. Sareen et al. (2013) showed that gas-phase compounds such as methylglyoxal can act as surfactants, which depress surface tension and enhance CCN-activity (and hygroscopicity). As methylglyoxal as well as other gas-phase surface-active compounds such as benzaldehyde and glyoxal are known products of toluene oxidation by OH (Hu et al., 2007; Baltaretu et al., 2009; Hamilton et al., 2005; White et al., 2014), it is likely that gas-phase surfactants are present here. If surfactant films are present on the non-denuded aerosol, enhancing their hygroscopicity, then desorption of the surfactants later upon heating may increase surface tension and depress apparent hygroscopicity. A monolayer of surfactant adsorbed from the gas phase would induce a negligible impact on bulk O : C or $\overline{OS}_C$, thus it is expected, as seen here, that the least volatile aerosol is the most oxidized. Altogether, this means that any relationship between hygroscopicity, oxidation state and volatility may be modulated by gas-phase compounds.

ACPD
14, 31441–31481, 2014

4 Conclusions

There is a strong relationship between exposure to OH and physicochemical properties for SOA formed from the oxidation of toluene and other small aromatic VOCs. Experiments with higher OH exposure showed higher SOA mass yields, more oxidized SOA, and reduced SOA volatility but only modest differences in hygroscopicity. Volatility varied by a factor of 30 for different OH exposure, and a ten-fold decrease in volatility was associated with a 0.5 increase in carbon oxidation state. The SOA was relatively hygroscopic for organic material, with $0.1 < \kappa < 0.2$ and if anything a slightly negative relationship between kappa and oxidation state, suggesting a possible role for surfactants. Organic nitrogen compounds were a major constituent in the SOA formed. Use of isotopically labeled toluene revealed that the methyl carbon atom of toluene is about three times less likely than the aromatic carbon atoms to form organic acids in these photo-oxidation reactions.

While individual experiments with different OH exposure revealed clear aging effects, these effects were generally not evident within a single experiment, even with photo-oxidation extending over many hours. This dichotomy remains a puzzle, suggesting that a complex interplay exists between gas-phase processes, including oxidation reactions that both functionalize and fragment condensable organic species as well as photolysis of some species.

Photochemical aging clearly influences anthropogenic SOA, and the general trend toward increased SOA mass and reduced volatility is consistent with progressive oxidation driving organic aerosol toward the highly oxidized, low-volatility endpoint observed around the world. However, especially for aromatic compounds, the specific mechanistic steps along this path remain enigmatic.

The Supplement related to this article is available online at doi:10.5194/acpd-14-31441-2014-supplement.

ACPD
14, 31441–31481, 2014

Acknowledgements. This work was supported by the EPA STAR program (grant RD-835405) and the Department of Energy Atmospheric Science Research Program (ASR grant DESC0007075). The high-resolution AMS was purchased with funds from NSF Major Research Instrumentation (CBET0922643) and the Wallace Research Foundation.

References

Alfarra, M. R., Good, N., Wyche, K. P., Hamilton, J. F., Monks, P. S., Lewis, A. C., and McFiggans, G.: Water uptake is independent of the inferred composition of secondary aerosols derived from multiple biogenic VOCs, Atmos. Chem. Phys., 13, 11769–11789, doi:10.5194/acp-13-11769-2013, 2013.

Allan, J. D., Delia, A. E., Coe, H., Bower, K. N., Alfarra, M. R., Jimenez, J. L., Middlebrook, A. M., Drewnick, F., Onasch, T. B., Canagaratna, M. R., Jayne, J. T., and Worsnop, D. R.: A generalised method for the extraction of chemically resolved mass spectra from Aerodyne aerosol mass spectrometer data, J. Aerosol Sci., 35, 909–922, doi:10.1016/j.jaerosci.2004.02.007, 2004.

Asa-Awuku, A., Sullivan, A. P., Hennigan, C. J., Weber, R. J., and Nenes, A.: Investigation of molar volume and surfactant characteristics of water-soluble organic compounds in biomass burning aerosol, Atmos. Chem. Phys., 8, 799–812, doi:10.5194/acp-8-799-2008, 2008.

Baltaretu, C. O., Lichtman, E. I., Hadler, A. B., and Elrod, M. J.: Primary atmospheric oxidation mechanism for toluene., J. Phys. Chem. A, 113, 221–230, doi:10.1021/jp806841t, 2009.

Canagaratna, M. R., Jimenez, J. L., Kroll, J. H., Chen, Q., Kessler, S. H., Massoli, P., Hildebrandt Ruiz, L., Fortner, E., Williams, L. R., Wilson, K. R., Surratt, J. D., Donahue, N. M., Jayne, J. T., and Worsnop, D. R.: Elemental ratio measurements of organic compounds using aerosol mass spectrometry: characterization, improved calibration, and implications, Atmos. Chem. Phys. Discuss., 14, 19791–19835, doi:10.5194/acpd-14-19791-2014, 2014.

Cappa, C. D. and Wilson, K. R.: Multi-generation gas-phase oxidation, equilibrium partitioning, and the formation and evolution of secondary organic aerosol, Atmos. Chem. Phys., 12, 9505–9528, doi:10.5194/acp-12-9505-2012, 2012.

Cerully, K. M., Bougiatioti, A., Hite Jr., J. R., Guo, H., Xu, L., Ng, N. L., Weber, R., and Nenes, A.: On the link between hygroscopicity, volatility, and oxidation state of ambient and water-

ACPD
14, 31441–31481, 2014

soluble aerosol in the Southeastern United States, Atmos. Chem. Phys. Discuss., 14, 30835–30877, doi:10.5194/acpd-14-30835-2014, 2014.

Chang, R. Y.-W., Slowik, J. G., Shantz, N. C., Vlasenko, A., Liggio, J., Sjostedt, S. J., Leaitch, W. R., and Abbatt, J. P. D.: The hygroscopicity parameter (κ) of ambient organic aerosol at a field site subject to biogenic and anthropogenic influences: relationship to degree of aerosol oxidation, Atmos. Chem. Phys., 10, 5047–5064, doi:10.5194/acp-10-5047-2010, 2010.

DeCarlo, P. F., Kimmel, J. R., Trimborn, A. M., Northway, M. J., Jayne, J. T., Aiken, A. C., Gonin, M., Fuhrer, K., Horvath, T., Docherty, K. S., Worsnop, D. R., and Jimenez, J. L.: Field-deployable, high-resolution, Time-of-Flight Aerosol Mass Spectrometer, Anal. Chem., 78, 8281–8289, 2006.

Donahue, N. M., Kroll, J. H., Pandis, S. N., and Robinson, A. L.: A two-dimensional volatility basis set – Part 2: Diagnostics of organic-aerosol evolution, Atmos. Chem. Phys., 12, 615–634, doi:10.5194/acp-12-615-2012, 2012.

Donahue, N. M., Robinson, A. L., and Pandis, S. N.: Atmospheric organic particulate matter: from smoke to secondary organic aerosol, Atmos. Environ., 43, 94–106, 2009.

Engelhart, G. J., Asa-Awuku, A., Nenes, A., and Pandis, S. N.: CCN activity and droplet growth kinetics of fresh and aged monoterpene secondary organic aerosol, Atmos. Chem. Phys., 8, 3937–3949, doi:10.5194/acp-8-3937-2008, 2008.

Facchini, M. C., Mircea, M., Fuzzi, S., and Charlson, R. J.: Cloud albedo enhancement by surface-active organic solutes in growing droplets, Nature, 401, 257–259, doi:10.1038/45758, 1999.

Facchini, M. C., Decesari, S., Mircea, M., Fuzzi, S., and Loglio, G.: Surface tension of atmospheric wet aerosol and cloud/fog droplets in relation to their organic carbon content and chemical composition, Atmos. Environ., 34, 4853–4857, doi:10.1016/S1352-2310(00)00237-5, 2000.

Farmer, D. K., Matsunaga, A., Docherty, K. S., Surratt, J. D., Seinfeld, J. H., Ziemann, P. J., and Jimenez, J. L.: Response of an aerosol mass spectrometer to organonitrates and organosulfates and implications for atmospheric chemistry, P. Natl. Acad. Sci. USA, 107, 6670–6675, doi:10.1073/pnas.0912340107, 2010.

Frosch, M., Bilde, M., DeCarlo, P. F., Juranyi, Z., Tritscher, T., Dommen, J., Donahue, N. M., Gysel, M., Weingartner, E., and Baltensperger, U.: Relating cloud condensation nuclei activity

ACPD
14, 31441–31481, 2014

and oxidation level of α-pinene secondary organic aerosols, J. Geophys. Res., 116, D2212, doi:10.1029/2011JD016401, 2011.

De Gouw, J. A., Goldan, P. D., Warneke, C., Kuster, W. C., Roberts, J. M., Marchewka, M., Bertman, S. B., Pszenny, A. A. P., and Keene, W. C.: Validation of proton transfer reaction-mass spectrometry (PTR-MS) measurements of gas-phase organic compounds in the atmosphere during the New England Air Quality Study (NEAQS) in 2002, J. Geophys. Res., 108, 4682, doi:10.1029/2003JD003863, 2003.

Hallquist, M., Wenger, J. C., Baltensperger, U., Rudich, Y., Simpson, D., Claeys, M., Dommen, J., Donahue, N. M., George, C., Goldstein, A. H., Hamilton, J. F., Herrmann, H., Hoffmann, T., Iinuma, Y., Jang, M., Jenkin, M. E., Jimenez, J. L., Kiendler-Scharr, A., Maenhaut, W., McFiggans, G., Mentel, Th. F., Monod, A., Prévôt, A. S. H., Seinfeld, J. H., Surratt, J. D., Szmigielski, R., and Wildt, J.: The formation, properties and impact of secondary organic aerosol: current and emerging issues, Atmos. Chem. Phys., 9, 5155–5236, doi:10.5194/acp-9-5155-2009, 2009.

Heald, C. L., Jacob, D. J., Park, R. J., Russell, L. M., Huebert, B. J., Seinfeld, J. H., Liao, H., and Weber, R. J.: A large organic aerosol source in the free troposphere missing from current models, Geophys. Res. Lett., 32, L18809, doi:10.1029/2005GL023831, 2005.

Hildebrandt, L., Donahue, N. M., and Pandis, S. N.: High formation of secondary organic aerosol from the photo-oxidation of toluene, Atmos. Chem. Phys., 9, 2973–2986, doi:10.5194/acp-9-2973-2009, 2009.

Hildebrandt, L., Henry, K., Kroll, J. H., Pandis, S. N., and Donahue, N. M.: Evaluating the mixing of organic aerosol components using high-resolution aerosol mass spectrometry, Environ. Sci. Technol., 45, 6329–6335, 2011.

Hildebrandt, L., Kostenidou, E., Mihalopoulos, N., Worsnop, D. R., Donahue, N. M., and Pandis, S. N.: Formation of highly oxygenated organic aerosol in the atmosphere: insights from the Finokalia Aerosol Measurement Experiments, Geophys. Res. Lett., 37, L23801, doi:10.1029/2010GL045193, 2010.

Jimenez, J. L., Canagaratna, M. R., Donahue, N. M., Prevot, A. S. H., Zhang, Q., Kroll, J. H., DeCarlo, P. F., Allan, J. D., Coe, H., Ng, N. L., Aiken, A. C., Docherty, K. S., Ulbrich, I. M., Grieshop, A. P., Robinson, A. L., Duplissy, J., Smith, J. D., Wilson, K. R., Lanz, V. A., Hueglin, C., Sun, Y. L., Tian, J., Laaksonen, A., Raatikainen, T., Rautiainen, J., Vaattovaara, P., Ehn, M., Kulmala, M., Tomlinson, J. M., Collins, D. R., Cubison, M. J., Dunlea, E. J., Huffman, J. a, Onasch, T. B., Alfarra, M. R., Williams, P. I., Bower, K., Kondo, Y.,

ACPD
14, 31441–31481, 2014

Schneider, J., Drewnick, F., Borrmann, S., Weimer, S., Demerjian, K., Salcedo, D., Cottrell, L., Griffin, R., Takami, A., Miyoshi, T., Hatakeyama, S., Shimono, A., Sun, J. Y., Zhang, Y. M., Dzepina, K., Kimmel, J. R., Sueper, D., Jayne, J. T., Herndon, S. C., Trimborn, A. M., Williams, L. R., Wood, E. C., Middlebrook, A M., Kolb, C. E., Baltensperger, U., and Worsnop, D. R.: Evolution of organic aerosols in the atmosphere, Science, 326, 1525–1529, doi:10.1126/science.1180353, 2009.

Kanakidou, M., Seinfeld, J. H., Pandis, S. N., Barnes, I., Dentener, F. J., Facchini, M. C., Van Dingenen, R., Ervens, B., Nenes, A., Nielsen, C. J., Swietlicki, E., Putaud, J. P., Balkanski, Y., Fuzzi, S., Horth, J., Moortgat, G. K., Winterhalter, R., Myhre, C. E. L., Tsigaridis, K., Vignati, E., Stephanou, E. G., and Wilson, J.: Organic aerosol and global climate modelling: a review, Atmos. Chem. Phys., 5, 1053–1123, doi:10.5194/acp-5-1053-2005, 2005.

King, S. M., Rosenoern, T., Shilling, J. E., Chen, Q., and Martin, S. T.: Increased cloud activation potential of secondary organic aerosol for atmospheric mass loadings, Atmos. Chem. Phys., 9, 2959–2971, doi:10.5194/acp-9-2959-2009, 2009.

Kostenidou, E., Pathak, R. K., and Pandis, S. N.: An algorithm for the calculation of secondary organic aerosol density combining AMS and SMPS data, Aerosol Sci. Tech., 41, 1002–1010, doi:10.1080/02786820701666270, 2007.

Kroll, J. H. and Seinfeld, J. H.: Chemistry of secondary organic aerosol: formation and evolution of low-volatility organics in the atmosphere, Atmos. Environ., 42, 3593–3624, doi:10.1016/j.atmosenv.2008.01.003, 2008.

Kroll, J. H., Smith, J. D., Che, D. L., Kessler, S. H., Worsnop, D. R., and Wilson, K. R.: Measurement of fragmentation and functionalization pathways in the heterogeneous oxidation of oxidized organic aerosol, Phys. Chem. Chem. Phys., 11, 8005–8014, 2009.

Kroll, J. H., Donahue, N. M., Jimenez, J. L., Kessler, S. H., Canagaratna, M. R., Wilson, K. R., Altieri, K. E., Mazzoleni, L. R., Wozniak, A. S., Bluhm, H., Mysak, E. R., Smith, J. D., Kolb, C. E., and Worsnop, D. R.: Carbon oxidation state as a metric for describing the chemistry of atmospheric organic aerosol, Nat. Chem., 3, 133–139, doi:10.1038/nchem.948, 2011.

Lambe, A. T., Onasch, T. B., Massoli, P., Croasdale, D. R., Wright, J. P., Ahern, A. T., Williams, L. R., Worsnop, D. R., Brune, W. H., and Davidovits, P.: Laboratory studies of the chemical composition and cloud condensation nuclei (CCN) activity of secondary organic aerosol (SOA) and oxidized primary organic aerosol (OPOA), Atmos. Chem. Phys., 11, 8913–8928, doi:10.5194/acp-11-8913-2011, 2011.

ACPD
14, 31441–31481, 2014

Lathem, T. L., Beyersdorf, A. J., Thornhill, K. L., Winstead, E. L., Cubison, M. J., Hecobian, A., Jimenez, J. L., Weber, R. J., Anderson, B. E., and Nenes, A.: Analysis of CCN activity of Arctic aerosol and Canadian biomass burning during summer 2008, Atmos. Chem. Phys., 13, 2735–2756, doi:10.5194/acp-13-2735-2013, 2013.

Lee, B.-H. and Pandis, S. N.: Volatility of Atmospheric Organic Aerosol, Carnegie Mellon University, Pittsburgh, 2010.

Lee, B. H., Kostenidou, E., Hildebrandt, L., Riipinen, I., Engelhart, G. J., Mohr, C., DeCarlo, P. F., Mihalopoulos, N., Prevot, A. S. H., Baltensperger, U., and Pandis, S. N.: Measurement of the ambient organic aerosol volatility distribution: application during the Finokalia Aerosol Measurement Experiment (FAME-2008), Atmos. Chem. Phys., 10, 12149–12160, doi:10.5194/acp-10-12149-2010, 2010.

Li, Z., Schwier, A. N., Sareen, N., and McNeill, V. F.: Reactive processing of formaldehyde and acetaldehyde in aqueous aerosol mimics: surface tension depression and secondary organic products, Atmos. Chem. Phys., 11, 11617–11629, doi:10.5194/acp-11-11617-2011, 2011.

Lim, Y. B., Tan, Y., and Turpin, B. J.: Chemical insights, explicit chemistry, and yields of secondary organic aerosol from OH radical oxidation of methylglyoxal and glyoxal in the aqueous phase, Atmos. Chem. Phys., 13, 8651–8667, doi:10.5194/acp-13-8651-2013, 2013.

Massoli, P., Lambe, A. T., Ahern, A. T., Williams, L. R., Ehn, M., Mikkilä, J., Canagaratna, M. R., Brune, W. H., Onasch, T. B., Jayne, J. T., Petäjä, T., Kulmala, M., Laaksonen, A., Kolb, C. E., Davidovits, P., and Worsnop, D. R.: Relationship between aerosol oxidation level and hygroscopic properties of laboratory generated secondary organic aerosol (SOA) particles, Geophys. Res. Lett., 37, L24801, doi:10.1029/2010GL045258, 2010.

Moore, R. H. and Nenes, A.: Scanning flow CCN analysis – a method for fast measurements of CCN spectra, Aerosol Sci. Tech., 43, 1192–1207, 2009.

Moore, R. H., Nenes, A., and Medina, J.: Scanning mobility CCN analysis – a method for fast measurements of size-resolved CCN distributions and activation kinetics, Aerosol Sci. Tech., 44, 861–871, doi:10.1080/02786826.2010.498715, 2010.

Padró, L. T., Asa-Awuku, A., Morrison, R., and Nenes, A.: Inferring thermodynamic properties from CCN activation experiments: single-component and binary aerosols, Atmos. Chem. Phys., 7, 5263–5274, doi:10.5194/acp-7-5263-2007, 2007.

Padro, L. T., Tkacik, D., Lathem, T., Hennigan, C. J., Sullivan, A. P., Weber, R. J., Huey, L. G., and Nenes, A.: Investigation of cloud condensation nuclei properties and droplet growth

ACPD
14, 31441–31481, 2014

kinetics of the water-soluble aerosol fraction in Mexico City, J. Geophys. Res., 115, D09204, doi:10.1029/2009JD013195, 2010.
Petters, M. D. and Kreidenweis, S. M.: A single parameter representation of hygroscopic growth and cloud condensation nucleus activity, Atmos. Chem. Phys., 7, 1961–1971, doi:10.5194/acp-7-1961-2007, 2007.
Ruehl, C. R., Chuang, P. Y., and Nenes, A.: Aerosol hygroscopicity at high (99 to 100 %) relative humidities, Atmos. Chem. Phys., 10, 1329–1344, doi:10.5194/acp-10-1329-2010, 2010.
Ruehl, C. R., Chuang, P. Y., Nenes, A., Cappa, C. D., Kolesar, K. R., and Goldstein, A. H.: Strong evidence of surface tension reduction in microscopic aqueous droplets, Geophys. Res. Lett., 39, L23801, doi:10.1029/2012GL053706, 2012.
Sareen, N., Schwier, A. N., Shapiro, E. L., Mitroo, D., and McNeill, V. F.: Secondary organic material formed by methylglyoxal in aqueous aerosol mimics, Atmos. Chem. Phys., 10, 997–1016, doi:10.5194/acp-10-997-2010, 2010.
Sareen, N., Schwier, A. N., Lathem, T. L., Nenes, A., and McNeill, V. F.: Surfactants from the gas phase may promote cloud droplet formation, P. Natl. Acad. Sci. USA, 110, 2723–2728, doi:10.1073/pnas.1204838110, 2013.
Shrivastava, M. K., Zelenyuk, A., Imre, D., Easter, R. C., Beranek, J., Zaveri, R. A., and Fast, J. D.: Implications of low volatility SOA and gas-phase fragmentation reactions on SOA loadings and their spatial and temporal evolution in the atmosphere, J. Geophys. Res.-Atmos., 118, 3328–3342, doi:10.1002/jgrd.50160, 2013.
Shulman, M. L., Jacobson, M. C., Carlson, R. J., Synovec, R. E., and Young, T. E.: Dissolution behavior and surface tension effects of organic compounds in nucleating cloud droplets, Geophys. Res. Lett., 23, 277–280, doi:10.1029/95GL03810, 1996.
Topping, D. O., McFiggans, G. B., Kiss, G., Varga, Z., Facchini, M. C., Decesari, S., and Mircea, M.: Surface tensions of multi-component mixed inorganic/organic aqueous systems of atmospheric significance: measurements, model predictions and importance for cloud activation predictions, Atmos. Chem. Phys., 7, 2371–2398, doi:10.5194/acp-7-2371-2007, 2007.
Volkamer, R., Jimenez, J. L., San Martini, F., Dzepina, K., Zhang, Q., Salcedo, D., Molina, L. T., Worsnop, D. R., and Molina, M. J.: Secondary organic aerosol formation from anthropogenic air pollution: rapid and higher than expected, Geophys. Res. Lett., 33, L17811, doi:10.1029/2006GL026899, 2006
Zhang, Q., Jimenez, J. L., Canagaratna, M. R., Allan, J. D., Coe, H., Ulbrich, I., Alfarra, M. R., Takami, A., Middlebrook, A. M., Sun, Y. L., Dzepina, K., Dunlea, E., Docherty, K., De-

ACPD
14, 31441–31481, 2014

Carlo, P. F., Salcedo, D., Onasch, T., Jayne, J. T., Miyoshi, T., Shimono, A., Hatakeyama, S., Takegawa, N., Kondo, Y., Schneider, J., Drewnick, F., Borrmann, S., Weimer, S., Demerjian, K., Williams, P., Bower, K., Bahreini, R., Cottrell, L., Griffin, R. J., Rautiainen, J., Sun, J. Y., Zhang, Y. M., and Worsnop, D. R.: Ubiquity and dominance of oxygenated species in organic aerosols in anthropogenically-influenced Northern Hemisphere midlatitudes, Geophys. Res. Lett., 34, L13801, doi:10.1029/2007gl029979, 2007.

ACPD
14, 31441–31481, 2014

Table 1. Experimental conditions.

Expt. #	Seeds[a]	$[Toluene]_0$[b] (ppb)	HONO injections	Lights (%)	[OH] exposure[c] ($cm^{-3}\ s^{-1}$)	Notes
1	Yes	~ 300	1	30	na	
2	No	~ 200	1+1	100	na	
3	Yes	~ 300	1+1	100	na	
4	No	~ 200	2	100	na	
5	Yes	~ 100	2+1	100	na	
6	No	~ 100	2	100	na	also o-xylene, trimethylbenzene, benzene
7	Yes	~ 1000	1	100	3.1×10^{10}	
8	Yes	~ 100	1	100	10×10^{10}	also p-xylene, ethylbenzene
9	Yes	~ 100	3+3	100	24×10^{10}	

[a] $(NH_4)_2SO_4$ seed particles were used in some experiments.
[b] VOC concentration estimated based on volume of VOC injected.
[c] Total OH exposure over the course of the experiment, estimated from exponential fits to the decay of toluene.
Data not available for experiments 1–6 due to lack of PTR-MS data.

ACPD
14, 31441–31481, 2014

Table 2. Summary of organic aerosol composition.

Expt #	$(NO + NO_2)/OA$[a]	$\overline{OS}_C$[b]	O : C	NO/NO_2[c]	$H_2O/(CO_2 + {}^{13}CO_2)$	$^{13}CO/{}^{13}CO_2$[c]	$CO_2/{}^{13}CO_2$[c]	Volatility Reduction (25 s)[e]	Volatility Reduction (15 s)[e]
1	0.10	−0.14	0.84	8.2	1.70	1.17	0.054	3.5	3.6
2	0.11	0.45	0.83	7.5	0.30	1.09	0.009	30.4	30.8
3	0.10	0.00	1.04	8.3	2.35	1.23	0.055	3.1	3.6
4	0.12	0.01	0.92	7.9	1.70	1.22	0.043	3.5	4.0
5	0.12	−0.14	0.94	8.0	2.10	1.22	0.078	1.9	2.2
6	0.10	−0.17	0.89	8.6	1.99	1.36	2.357	1.7	2.5
7	0.13	−0.29	0.76	8.2	1.85	N/A[d]	N/A[d]	1.0	1.0
8	0.10	−0.05	0.94	7.3	1.67	1.13	1.812	4.3	4.9
9	0.12	−0.04	1.02	7.0	2.40	1.13	0.072	6.2	8.2

[a] After first period of lights on. OA includes the sum $(NO + NO_2)$.
[b] After first period of lights on, $\overline{OS}_C$ approximated as $2 \times O : C - H : C$.
[c] From linear regressions throughout the experiment (when OA present).
[d] Not applicable (no isotopically labeled VOC used in experiment 7).
[e] Volatility reduction estimated for data collected at residence times of 15 and 25 s. Values are calculated relative to experiment 7 which featured the highest volatility.

ACPD
14, 31441–31481, 2014

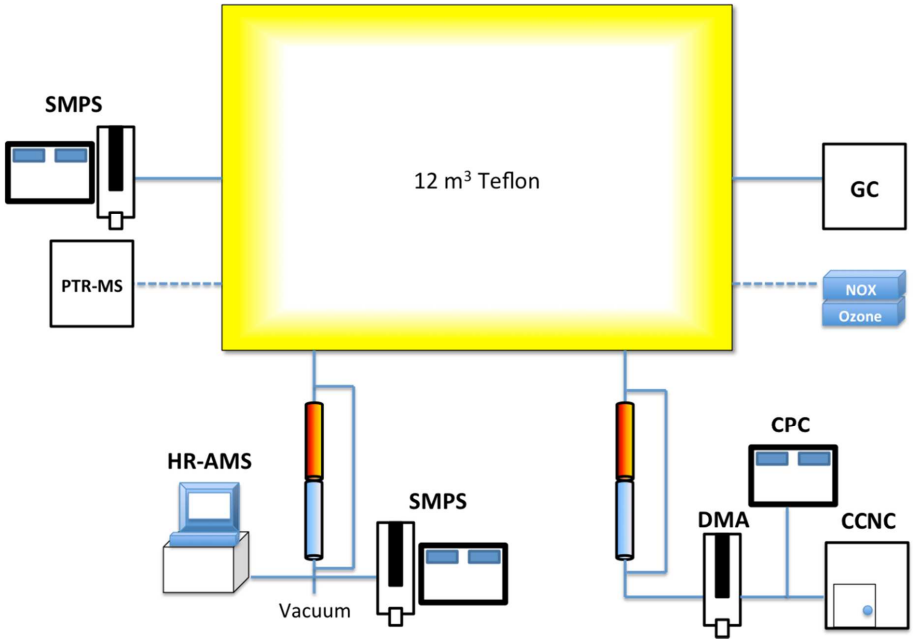

Figure 1. Schematic of experimental set-up. Dotted lines indicate that the equipment was used in selected experiments.

ACPD
14, 31441–31481, 2014

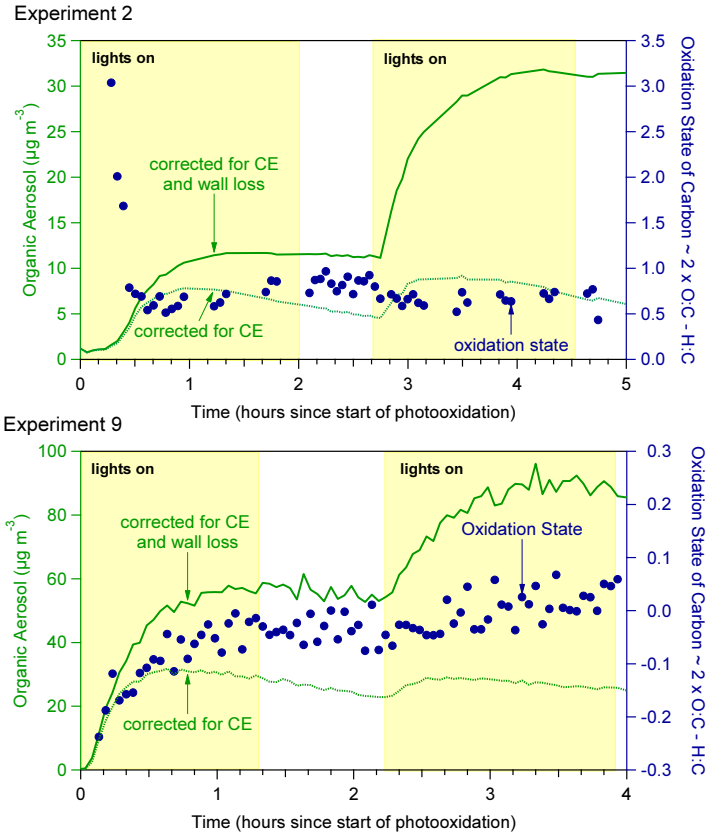

Figure 2. Time series of OA concentration (corrected for CE and corrected for CE and wall loss) from an unseeded experiment (2, top) and a seeded experiment (9, bottom), both with two photo-oxidation periods ("lights on") before which HONO was injected. The periods during which the reactor was dark are shown with white background while the periods with UV-lights are shaded yellow. Also shown is the OA oxidation state (right axis).

ACPD
14, 31441–31481, 2014

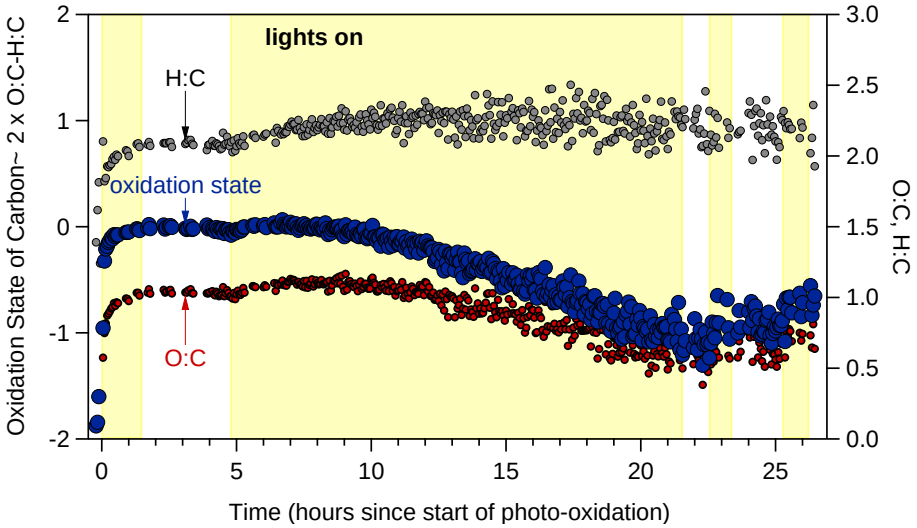

Figure 3. Time series of oxidation state (left axis) and elemental ratios of O : C and H : C (right axis) for experiment 3. The periods during which the reactor was dark are shown in with white background while the periods with UV-lights are shaded yellow.

ACPD
14, 31441–31481, 2014

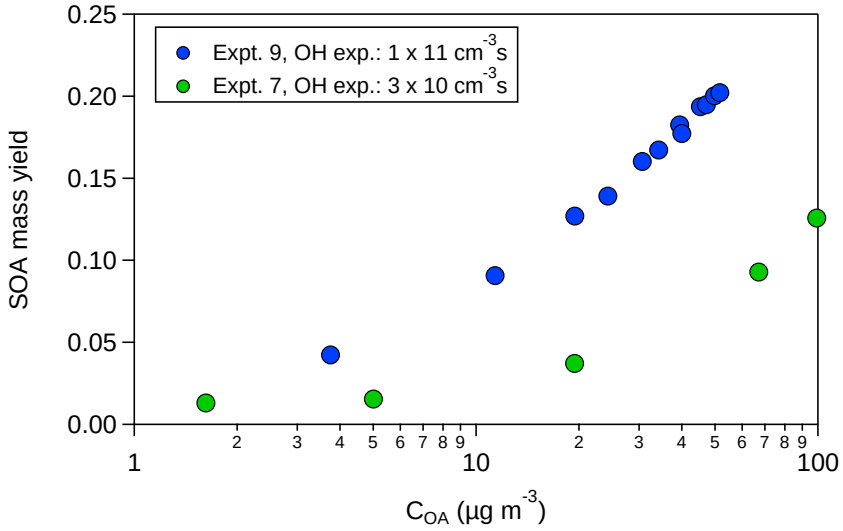

Figure 4. Organic aerosol mass yields for Expts. 7 and 9.

ACPD
14, 31441–31481, 2014

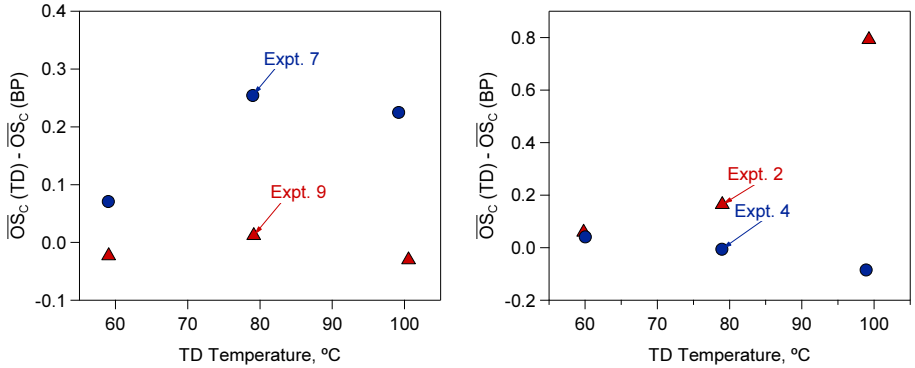

Figure 5. Comparison of the difference in oxidation state of denuded and total OA vs. TD temperature for two seeded experiments (7 and 9, left panel) and two unseeded experiments (2 and 4, right panel). For OA of intermediate oxidation state (around 0, Expts. 9 and 4), oxidation state of the denuded OA is similar to the oxidation state of the full OA, implying that oxidation state does not correlate significantly with volatility. For OA of higher or lower oxidation state (Expts. 2 and 7, respectively) oxidation state anti-correlates with volatility, shown here as an increase in oxidation state difference with TD temperature.

ACPD
14, 31441–31481, 2014

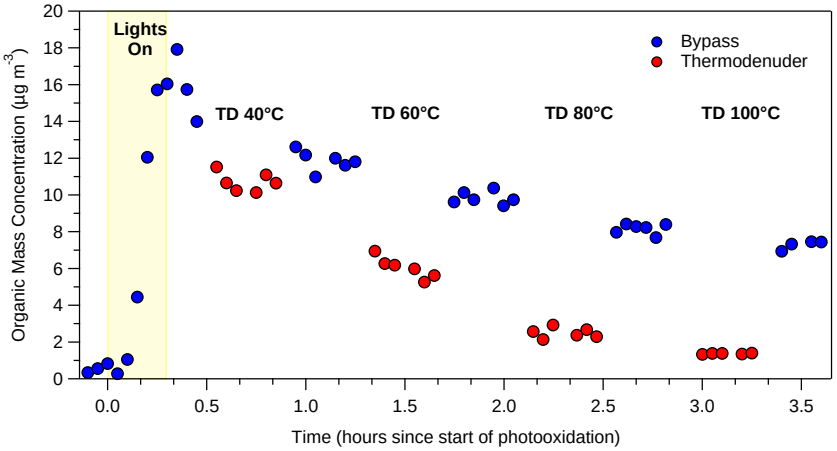

Figure 6. Bypass (blue) and thermodenuder (red) organic mass concentration timeseries for Experiment 7. The yellow shaded region denotes time when the UV lights were on. Temperatures represent the TD setpoint temperature. The bypass data have not been corrected for losses to the walls of the chamber. The TD measurements have not been corrected for losses in the TD.

ACPD
14, 31441–31481, 2014

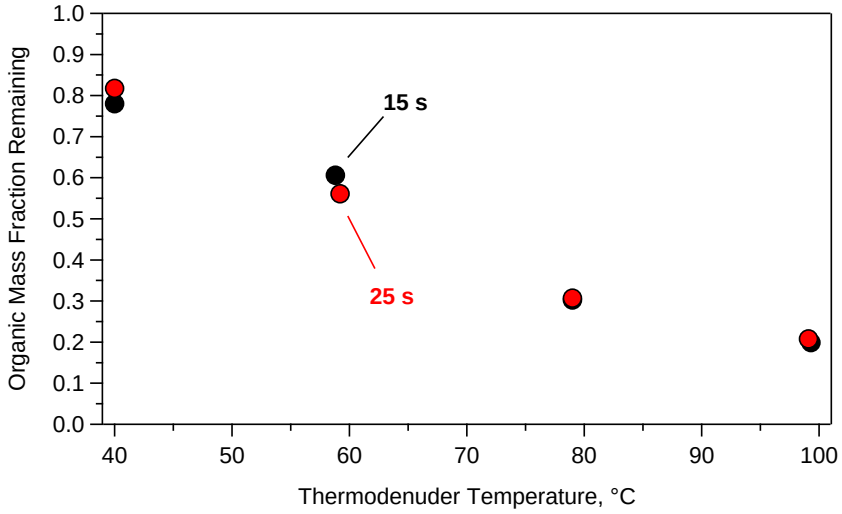

Figure 7. Organic mass fraction remaining as a function of thermodenuder temperature at a residence time of 15 s (black) and 25 s (red) for Experiment 7. Thermograms have been corrected for TD losses.

ACPD
14, 31441–31481, 2014

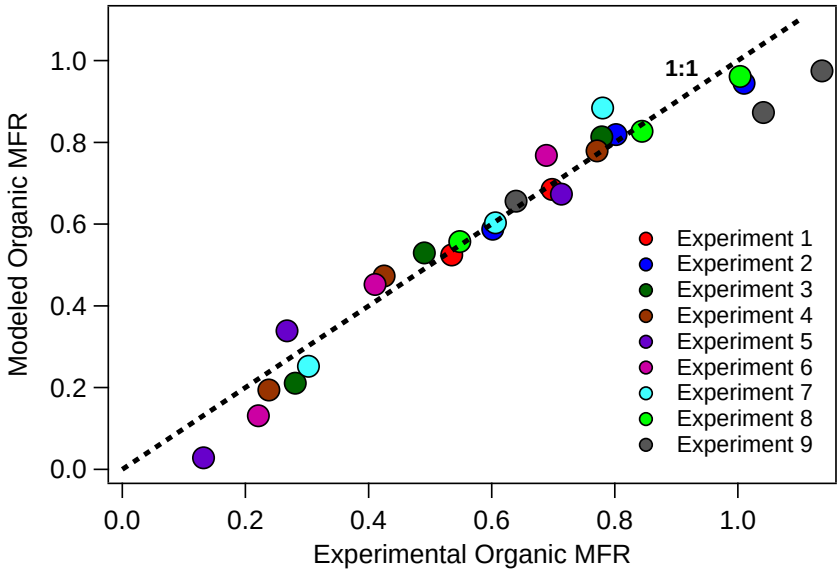

Figure 8. Comparison of the predicted MFRs based on the best fits and the experimental values at 15 s for all temperatures for all experiments.

ACPD
14, 31441–31481, 2014

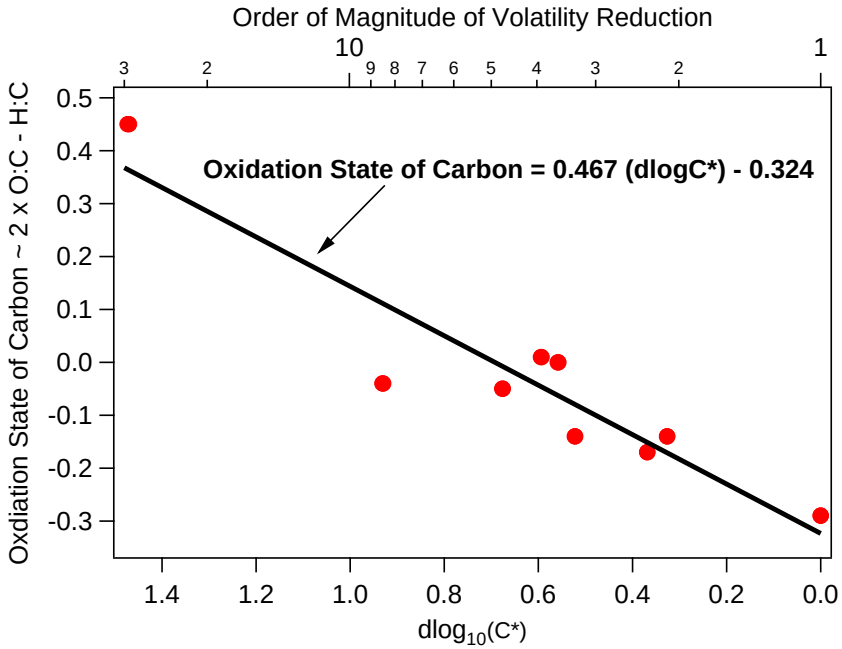

Figure 9. Oxidation state and volatility reduction in terms of change of $\log C^*$ for the toluene SOA system. Red circles represent a single experiment and a single best-fit (black) line shows the trend.

ACPD
14, 31441–31481, 2014

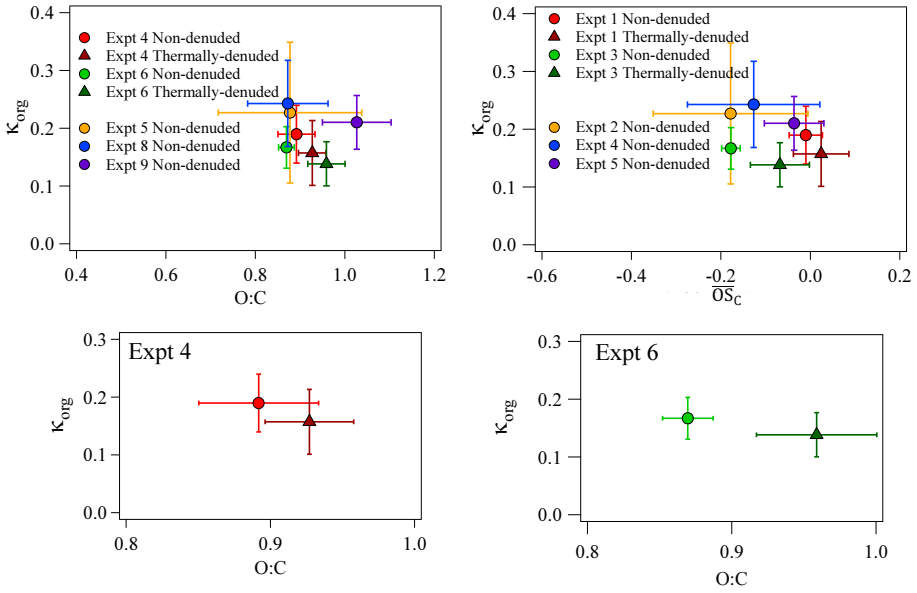

Figure 10. κ_{org} vs. O : C (top, left) and $\overline{OS}_C$ (top, right) for all experiments as listed in Table 1. Also shown are magnified hygroscopicity and O : C for unseeded experiments with non-denuded and thermally-denuded measurements (bottom). Vertical and horizontal error bars represent the SD in κ_{org} and O : C or $\overline{OS}_C$, respectively.

ACPD
14, 31441–31481, 2014